Orbital Edelstein effect from density-wave order

Geremia Massarelli, Bryce Wu, and Arun Paramekanti
Department of Physics, University of Toronto, Toronto, Ontario, Canada M5S 1A7

(Received 17 April 2019; published 16 August 2019)

Coupling between charge and spin, and magnetoelectric effects more generally, have been an area of great interest for several years, with the sought-after ability to control magnetic degrees of freedom via charge currents serving as an impetus. The orbital Edelstein effect (OEE) is a kinetic magnetoelectric effect consisting of a bulk orbital magnetization induced by a charge current. It is the orbital analog of the spin Edelstein effect in spin-orbit coupled materials, in which a charge current drives nonzero electron spin magnetization. The OEE has recently been investigated in the context of Weyl semimetals and Weyl metals. Motivated by these developments, we study a model of electrons without spin-orbit coupling which exhibits line nodes protected by nonsymmorphic glide symmetries that get gapped out via symmetry breaking due to an interaction-induced charge density wave order. This model is shown to exhibit a temperature dependent OEE, which appears due to symmetry reduction into a nonchiral, yet gyrotropic, crystal class. We present a solenoid picture for this emergent OEE that arises from broken glide and inversion symmetries.

DOI: 10.1103/PhysRevB.100.075136

I. INTRODUCTION

The field of magnetoelectric effects has seen a revival in interest in the past decades on several fronts. The discovery and study of multiferroicity in correlated materials has uncovered unconventional mechanisms which can give rise to a large effective magnetoelectric coupling [1–8]. Similarly, the discovery of three-dimensional (3D) topological insulators has led to an exploration of novel magnetoelectric effects due to emergent axion electrodynamics in such topological phases [9–18]. The wide interest in such magnetoelectric effects stems partly from the technological potential of controlling charge degrees of freedom via magnetic fields or, conversely, tuning magnetism via an applied electric field.

A prominent example of such a magnetoelectric effect is the nonequilibrium phenomenon of current-induced magnetization, which is also termed *kinetic magnetoelectric effect* (KME) [19,20]. The intrinsic-spin variant of this effect, wherein a charge current in a spin-orbit-coupled conductor gives rise to bulk spin polarization and, hence, a net magnetization, is referred to as the *Edelstein effect* or the *inverse spin-galvanic effect* [21,22] and has been under study for several decades [23]. A great deal of experimental work has focused on the Edelstein effect in 2D systems, notably in thin-film semiconductors [24–29] and at metal surfaces [30]. However, experiments on 3D materials have been scant, although some recent studies have reported its observation in trigonal tellurium [31,32].

In recent years, it has come to light that 3D systems can have an intrinsic orbital contribution to the KME, analogous to the spin part and arising as a consequence of the orbital magnetic moment of Bloch bands [20,33–40], notably in trigonal selenium and tellurium. Whereas the ordinary Edelstein effect (hereafter referred to as the *spin* Edelstein effect, SEE) relies on crystalline spin-orbit coupling (SOC) to give Bloch states a spin texture and, hence, is limited by the size of the SOC, the *orbital Edelstein effect* (OEE), also referred to as the *inverse gyrotropic magnetic effect* [34], is determined solely by the geometry of the crystal [33,36].

Chiral crystals are a subset of those that can exhibit the KME. Previous studies have considered trigonal selenium and tellurium and viewed their chiral nature as descending from a charge-density-wave (CDW) instability of a hypothetical parent phase [41], and others have studied optical gyrotropy as a probe for symmetry breaking in the chiral CDW phase of $1T$-$TiSe_2$ [42] and in stripe-ordered cuprates [43]. It has also been shown that Weyl nodes at the Fermi level can yield a large intrinsic contribution to the KME [33,36].

Our work builds on this theme and explores the KME induced by symmetry breaking in a system with line nodes protected by nonsymmorphic symmetries in the electronic band structure. The resulting phase is a nonchiral but gyrotropic crystal, and we study the concomitant temperature-dependent KME as a probe of the density-wave order. Below, we briefly review the OEE, before introducing our model Hamiltonian and presenting its theoretical study. Our work suggests that line node semimetals which are weakly gapped by charge order might be a promising place to search for large OEE.

II. ORBITAL EDELSTEIN EFFECT

Electrons in crystalline solids form Bloch bands with an intrinsic spin magnetic moment

$$\mathbf{s}_{\mathbf{k}n} = -\frac{ge}{2m_e}\langle u_{\mathbf{k}n}|\mathbf{s}|u_{\mathbf{k}n}\rangle, \tag{1}$$

where $\mathbf{s} = \hbar\boldsymbol{\sigma}/2$ is the spin operator for the electrons and the electron charge is $(-e)$. The modern theory of magnetization in solids [44–47] has discovered that such Bloch bands also

host an intrinsic orbital magnetic moment given by

$$\mathbf{m}_{\mathbf{k}n} = \frac{e}{2\hbar}\mathrm{Im}\,\langle\nabla_{\mathbf{k}}u_{\mathbf{k}n}|\times(H_{\mathbf{k}}-\varepsilon_{\mathbf{k}n})|\nabla_{\mathbf{k}}u_{\mathbf{k}n}\rangle, \tag{2}$$

where $H_{\mathbf{k}}$ is the Bloch Hamiltonian, n is the band index, and $H_{\mathbf{k}}|u_{\mathbf{k}n}\rangle = \varepsilon_{\mathbf{k}n}|u_{\mathbf{k}n}\rangle$. This orbital magnetization has been shown to arise from the self-rotation of wave packets in the semiclassical theory of electron dynamics [45,48]. Since $\mathbf{m}_{\mathbf{k}n} \to -\mathbf{m}_{-\mathbf{k}n}$ under time reversal and $\mathbf{m}_{\mathbf{k}n} \to \mathbf{m}_{-\mathbf{k}n}$ under spatial inversion, it is clear that at least one of these symmetries must be broken in order for $\mathbf{m}_{\mathbf{k}n}$ to not be identically zero.

From the viewpoint of semiclassical dynamics, given an electron distribution function $f_{\mathbf{k}n}$, the intrinsic contribution to the net electronic magnetization is given by [20,44,48]

$$\mathbf{M} = \frac{1}{\mathcal{V}}\sum_{\mathbf{k}n} f_{\mathbf{k}n}(\mathbf{m}_{\mathbf{k}n}+\mathbf{s}_{\mathbf{k}n}), \tag{3}$$

where $\mathcal{V}$ is the crystal volume. In thermodynamic equilibrium for a time-reversal symmetric system, the Fermi-Dirac distribution, $f^0_{\mathbf{k}n} = f(\varepsilon_{\mathbf{k}n}-\mu)$ forces zero a net magnetization $\mathbf{M}=0$ because of cancellation between contributions from opposite crystal momenta [36]. However, an asymmetric distribution function, such as that arising from an applied electric field, can generally give rise to nonzero net bulk magnetization.

Explicitly, to lowest order in an applied uniform DC electric field $\mathbf{E}$, the distribution function becomes [49]

$$f_{\mathbf{k}n} = f^0_{\mathbf{k}n} + e\tau(\mathbf{E}\cdot\mathbf{v}_{\mathbf{k}n})\left.\frac{df}{d\xi}\right|_{\xi=\varepsilon_{\mathbf{k}n}-\mu}, \tag{4}$$

where $\mathbf{v}_{\mathbf{k}n}$ is the electronic group velocity and τ is the impurity-scattering relaxation time in relaxation-time approximation. Hence, the magnetization arises as a linear response to an applied electric field,

$$M_\kappa = \alpha_{\kappa\lambda}E_\lambda, \tag{5}$$

with the linear response tensor

$$\alpha_{\kappa\lambda} = \alpha^{\mathrm{orb}}_{\kappa\lambda} + \alpha^{\mathrm{spin}}_{\kappa\lambda} \tag{6a}$$

$$= \tau e\frac{1}{\mathcal{V}}\sum_{\mathbf{k},n}\left.\frac{df}{d\xi}\right|_{\xi=\varepsilon_{\mathbf{k}n}-\mu}(m_{\mathbf{k}n,\kappa}+s_{\mathbf{k}n,\kappa})\,v_{\mathbf{k}n,\lambda}, \tag{6b}$$

where κ and λ are Cartesian indices. The tensors α^{spin} and α^{orb}, respectively, describe the SEE and the OEE.

The form of the tensor α is significantly constrained by crystal symmetry [23,36,50,51]. Indeed, α is an axial rank-two tensor since it relates a polar vector $\mathbf{E}$ to an axial vector $\mathbf{M}$. Crystal classes whose point-group symmetries allow for nonzero axial rank-two response tensors are known as *gyrotropic*. The reason for this name is that the tensor governing natural optical activity, or *gyrotropy*, transforms in the same way as α; thus KME and optical gyrotropy go hand in hand.

We note that the same symmetry constraints govern the appearance of nonzero spin and orbital contributions to α, so both are expected to arise together, and there is no clear route to disentangling them experimentally in a 3D system [32,36]. Indeed, the authors of Ref. [32] conclude by speculating that the current-induced magnetization they observe in trigonal tellurium may be due not only to the well-known SEE, but also to the OEE.

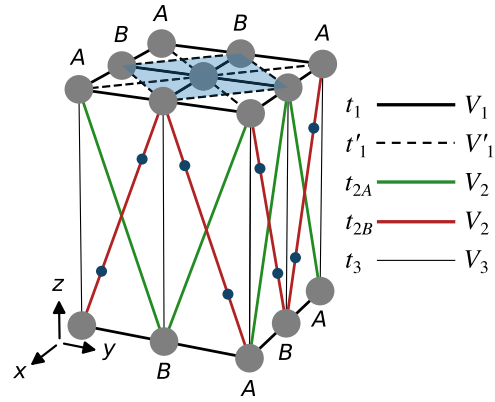

FIG. 1. Tetragonal crystal structure showing identical atoms (large gray spheres) on the A and B sublattices, with a legend for hopping amplitudes and repulsion strengths. Primitive translations $\mathbf{a}$, $\mathbf{b}$, and $\mathbf{c}$ are defined in the main text. The volume shown corresponds to two unit cells as defined in Sec. III, and the projection of the unit cell onto the x-y plane is shaded in blue. The secondary atoms (small dark-blue spheres) are *not* considered in the tight-binding model, as discussed in the main text.

III. MODEL

As an example of the OEE brought about by symmetry breaking, we consider a tight-binding toy model of electrons moving in the tetragonal crystal shown in Fig. 1, consisting of identical atoms arranged in layered square lattices. We assume a single isotropic orbital and ignore the electron spin hereafter; for this reason, there is no spin contribution to α in this work. There are many cases where this is a useful starting point. In crystals with density-wave order driven by nearest-neighbor (NN) electronic repulsion, such as we will consider below, both spin components behave in the same manner—including spin then only leads to an extra factor of two in certain equations below. The other case where spin may be ignored is in spin-polarized systems, which might be a useful description of states in a large energy interval around the Fermi energy in strong ferromagnets (i.e., in half-metals).

We define the x-y-plane NN lattice constant to be a_0 and the lattice constant along the stacking direction $\hat{\mathbf{z}}$ to be c. In the x-y planes, we include NN hopping t_1 and next-nearest-neighbor (NNN) hopping t'_1. In the y-z and z-x planes, we include NN hopping t_3 and the peculiar NNN hoppings depicted in Fig. 1, with $t_{2A} \neq t_{2B}$. Although the atoms are chemically identical, this last choice differentiates A and B sublattices, requiring us to use a two-atom unit cell with primitive translations $\mathbf{a} = a_0(\hat{\mathbf{x}}-\hat{\mathbf{y}})$, $\mathbf{b} = a_0(\hat{\mathbf{x}}+\hat{\mathbf{y}})$, and $\mathbf{c} = c\hat{\mathbf{z}}$. Hereafter, this unit cell is referred to as *the unit cell* and its first Brillouin zone, as *the first Brillouin zone*. The crystal's space group is $P4/nbm$, and its associated crystal class is $4/mmm$. Importantly, this crystal has centers of inversion at the middle point of every x-y-plane NN bond. We use the following values for the hopping parameters: $t'_1 = 0.7\,t_1$, $t_{2A} = 0.1\,t_1$, $t_{2B} = 0.4\,t_1$, and $t_3 = 0.5\,t_1$; we have checked that our results are qualitatively robust upon tuning these parameters.

The nonequivalence of the hopping amplitudes t_{2A} and t_{2B} giving rise to $P4/nbm$ symmetry may be rationalized as depicted in Fig. 1: If a secondary set of atoms (shown in dark blue) is present only along the red bonds—which would be consistent with the space-group symmetry of the model—and their energy levels are far from the Fermi energy, their dynamics could be integrated out, with the end result of renormalizing the hopping amplitude between the primary atoms (shown in gray), effectively leading to $t_{2A} \neq t_{2B}$. The same reasoning holds if there are additional secondary atoms on the green bonds *provided they are of a species different from those on the red bonds*.

As is true for any crystal class with inversion symmetry, $4/mmm$ is nongyrotropic [50,51]. However, if the symmetry of the crystal were to be reduced, for instance by the onset of CDW order, the inversion symmetry could be broken and, indeed, the ordered structure could fall into a gyrotropic class. Below, we first study the band structure of this model in the absence of interactions, before turning to the impact of electronic repulsion.

A. Noninteracting band structure

The noninteracting Hamiltonian is

$$K = \sum_{\alpha,\beta} \sum_{i,j} -t_{ij}^{\alpha\beta} c_i^{\alpha\dagger} c_j^{\beta}, \tag{7}$$

where $c_i^{\alpha\,\dagger}$ creates an electron on sublattice α of unit cell i (that is, on the atom at position $\mathbf{r}_i^{\alpha}$). In momentum space,

$$K = \sum_{\mathbf{k}} \psi_{\mathbf{k}}{}^{\dagger} \left(d_{\mathbf{k}}^0 + \vec{d}_{\mathbf{k}} \cdot \vec{\tau}\right) \psi_{\mathbf{k}}, \tag{8}$$

where $c_{\mathbf{k}}^{\alpha} = N^{-1/2} \sum_i \mathrm{e}^{-\mathrm{i}\mathbf{k}\cdot\mathbf{r}_i^{\alpha}} c_i^{\alpha}$, N is the number of unit cells, $\vec{\tau}$ is the vector of Pauli matrices (acting in sublattice space), and $\psi_{\mathbf{k}}{}^{\dagger} = (c_{\mathbf{k}}^{A\,\dagger} \;\; c_{\mathbf{k}}^{B\,\dagger})$. Because of time-reversal symmetry, the hopping amplitudes $t_{ij}^{\alpha\beta}$ are necessarily real valued. We will measure momenta in units of inverse lattice spacing, setting $a = c = 1$ henceforth. With this, we arrive at

$$d_{\mathbf{k}}^0 = -2t_3 \cos(k_c) - 2t_1' (\cos(k_a) + \cos(k_b)) \tag{9a}$$

$$d_{\mathbf{k}}^1 = -4 \cos\left(\frac{k_a}{2}\right) \cos\left(\frac{k_b}{2}\right) (t_1 + (t_{2A} + t_{2B}) \cos(k_c)) \tag{9b}$$

$$d_{\mathbf{k}}^2 = 4(t_{2A} - t_{2B}) \cos\left(\frac{k_a}{2}\right) \cos\left(\frac{k_b}{2}\right) \cos(k_c) \tag{9c}$$

$$d_{\mathbf{k}}^3 = 0. \tag{9d}$$

The product $\Pi\Theta$ of the aforementioned inversion symmetry Π with the Hamiltonian's time-reversal symmetry Θ constrains $d_{\mathbf{k}}^3 \equiv 0$ identically; for this reason, band touchings for this crystal will generically arise as line nodes, as seen in the noninteracting band structure (top panel of Fig. 6). More specifically, the nonsymmorphic symmetries present in the space group $P4/nbm$ give rise to band touchings along high-symmetry lines (see Appendix C); Fig. 2 shows the location of these lines in the Brillouin zone.

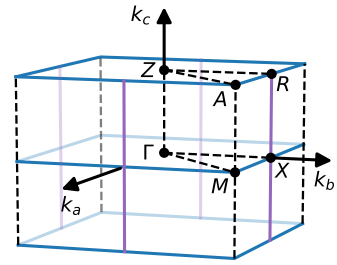

FIG. 2. Location of the line nodes (solid lines, shown in color) present in the symmetric phase within the first Brillouin zone as defined in Sec. III. High-symmetry points are labeled.

B. Repulsive interactions

Next, we include repulsive interactions between NNs and NNNs; that is,

$$V = \frac{1}{2} \sum_{(i,\alpha)\neq(j,\beta)} V_{ij}^{\alpha\beta} n_i^{\alpha} n_j^{\beta}, \tag{10}$$

where $n_i^{\alpha} = c_i^{\alpha\,\dagger} c_i^{\alpha}$ is the number operator for the atom (i,α) and we take $V_{ij}^{\alpha\beta} = V_{ji}^{\beta\alpha}$. We take nonzero repulsions $V_{ij}^{\alpha\beta}$ on the same bonds as the hopping amplitudes and use a similar naming scheme, as shown in Fig. 1. Note that, unlike for the hopping amplitudes $t_{2A} \neq t_{2B}$, we take the repulsion strengths to be V_2 on both the red and green bonds—this choice serves as a representative slice through the full parameter space and illustrates some of the key ideas. Hence, the full Hamiltonian is given by $H = K + V$ and has the same (nongyrotropic) space-group symmetry $P4/nbm$ as K.

Spontaneous symmetry breaking (SSB), however, could reduce the symmetry of the crystal. A simple scenario is a CDW phase in which the densities on the A and B atoms are unequal, in which case the space group becomes $P\bar{4}2m$, whose crystal class—$\bar{4}2m$—is gyrotropic.

We note that in the absence of spin order, a Hubbard term $U \sum_i n_{i\uparrow} n_{i\downarrow}$ would modify the mean-field (MF) Hamiltonian by a mere uniform offset in the chemical potential μ. Hence, as we will restrict ourselves to ansätze without spin order, we do not bother including the Hubbard interaction.

We performed a MF calculation of the CDW order in the above system, allowing for a finite set of commensurate wave vectors. The ordering wave vectors favored by the interaction were identified by considering a simple model of classical charges resting at each atomic site of the crystal of Fig. 1—see Appendix A. Based on this, the four ordering wave vectors included in the ansatz are

$$\mathbf{Q}_0 = 0, \quad \mathbf{Q}_1 = \pi\hat{\mathbf{a}} + \pi\hat{\mathbf{b}},$$
$$\mathbf{Q}_2 = \pi\hat{\mathbf{c}}, \quad \mathbf{Q}_3 = \pi\hat{\mathbf{a}} + \pi\hat{\mathbf{b}} + \pi\hat{\mathbf{c}}.$$

The order parameters for the mean-field theory are the Fourier amplitudes $\rho_{\mathbf{Q}}^{\alpha}$ for the $\mathbf{Q}$ listed above, where $\alpha \in \{A, B\}$. However, we find it convenient to express the amplitudes on the A and B sublattices in terms of a symmetric and an antisymmetric part, respectively defined as

$$\rho_{\mathbf{Q}}^{\mathrm{s}} := \frac{\rho_{\mathbf{Q}}^{A} + \rho_{\mathbf{Q}}^{B}}{2}, \tag{11a}$$

$$\rho_{\mathbf{Q}}^{\mathrm{a}} := \frac{\rho_{\mathbf{Q}}^{A} - \rho_{\mathbf{Q}}^{B}}{2}. \tag{11b}$$

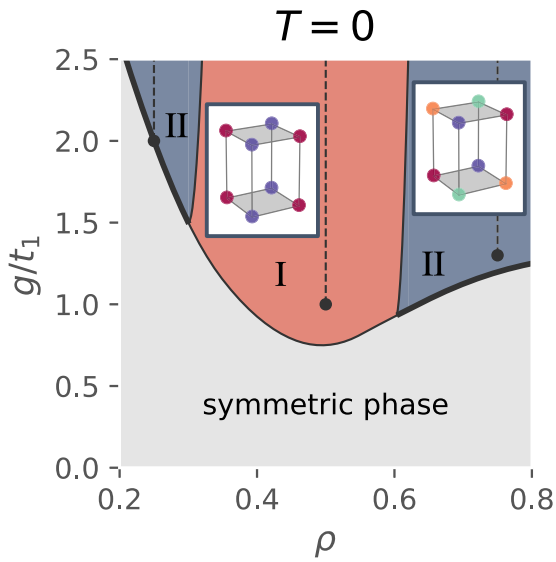

FIG. 3. CDW phases arising in the MF study as a function of the electronic filling ρ and g (which parametrizes the repulsion strength). Continuous and discontinuous transitions are, respectively, shown as thin and thick solid lines, while insulating lines, which occur at fillings 1/4, 1/2, and 3/4, are dashed. The nature of Phases I and II is described in the text.

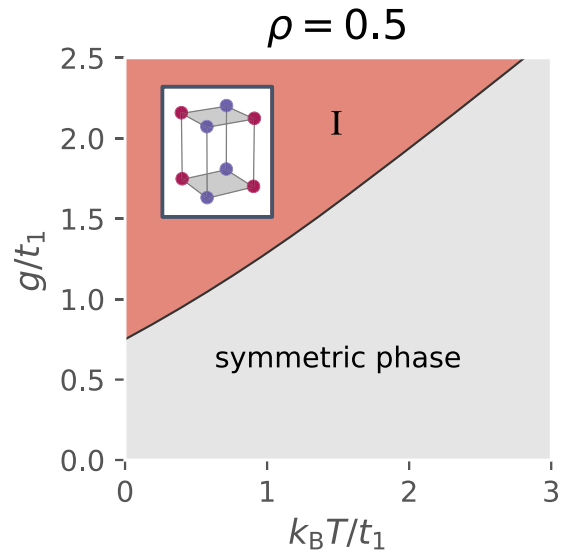

FIG. 4. CDW phases arising in the MF study at half filling ($\rho = 0.5$) as a function of temperature and g (which parametrizes the repulsion strength). The transition into Phase I from the symmetric phase is continuous. The nature of Phase I is described in the text.

Since $\rho^{s}_{\mathbf{Q}_0} = \rho$, the electron filling, we are left with seven independent MFs.

IV. RESULTS

A. Mean-field theory of charge-density-wave order

We focus on a cut of parameter space parametrized by g such that

$$V_1 = g, \quad V_1' = \frac{g}{2}, \quad V_2 = \frac{g}{2}, \quad V_3 = \frac{g}{2}. \tag{12}$$

According to the model of electrostatic charges, at these relative repulsion values (marked by a white star in Fig. 10), the interaction most favors an ordering with $\rho^{a}_{\mathbf{Q}_0} \neq 0$; however, the region of parameter space with $\rho^{\alpha}_{\mathbf{Q}_3} \neq 0$ most favored is nearby (see Appendix A).

The MF calculation, for which the zero-temperature phase diagram is shown in Fig. 3, does indeed identify a swath of pure $\rho^{a}_{\mathbf{Q}_0} \neq 0$ order for sufficiently large g and for approximately $0.3 < \rho < 0.6$—call this *Phase I*. In addition to this phase, at high and low filling, we discover regions where multiple CDW modes coexist (specifically, $\mathbf{Q}_0$ and $\mathbf{Q}_3$); that is, $\rho^{a}_{\mathbf{Q}_0} \neq 0$ and $\rho^{\alpha}_{\mathbf{Q}_3} \neq 0$ (where α is either A or B)—call these regions *Phase II*. The orders in these phases are depicted in insets to Fig. 3.

For $g/t_1 \gg 1$, we observe that the phase diagram is approximately symmetric under $\rho \to 0.5 - \rho$; this is expected given the particle-hole symmetry of V, which becomes an approximate symmetry of H when K is nonzero but small compared with V. The system is insulating at zero temperature along lines shown as dashed in the phase diagram. These lines are located at fillings 1/4, 1/2, and 3/4, and each terminate at a point corresponding to a metal-insulator transition at commensurate filling. We can qualitatively understand the appearance of these insulating phases at commensurate fillings as follows. The classical picture in Appendix A, appropriate in the large-g limit, favors the $\mathbf{Q}_0$ charge-ordered state for our choice of interaction parameters. It is pictorially clear from Fig. 3 that this ordered state can be a stable "atomic" insulator at 1/2 filling. However, at 1/4 and 3/4 filling, this charge-ordered state will continue to host a gapless Fermi surface. Instead, at these other commensurate fillings, it is advantageous to have a secondary $\mathbf{Q}_3$ order which doubles the unit cell, permitting a gapped lowest band, again stabilizing a simple "atomic" charge-ordered insulator as is again pictorially clear from Fig. 3. The phase diagram at $\rho = 0.5$ as a function of T and g is shown in Fig. 4 and reveals that raising the system temperature progressively suppresses Phase-I order.

B. Magnetoelectric response in Phase I

We study the temperature-dependent SSB-induced OEE in broken-symmetry Phase I, whose sole order parameter is $\rho^{a}_{\mathbf{Q}_0}$. The other phases of the mean-field theory, such as Phase II, involve additional breaking of translational symmetry; this enlarges the unit cell and leads to more bands, making the analysis less transparent. Figure 5 shows the evolution of $\rho^{a}_{\mathbf{Q}_0}$ and the components of the response tensor α^{orb} at half filling ($\rho = 0.5$) and fixed interaction strength ($g = 1.5\,t_1$). The phase transition, which is seen to be continuous, takes place at $k_B T_c \approx 1.4\,t_1$.

As alluded to previously, the point-group symmetry in Phase I is the $\bar{4}2m$, and a symmetry analysis (Appendix D) reveals that symmetry constrains the response tensor α to the form [50]

$$\alpha = \begin{pmatrix} \alpha_{aa} & & \\ & -\alpha_{aa} & \\ & & 0 \end{pmatrix}. \tag{13}$$

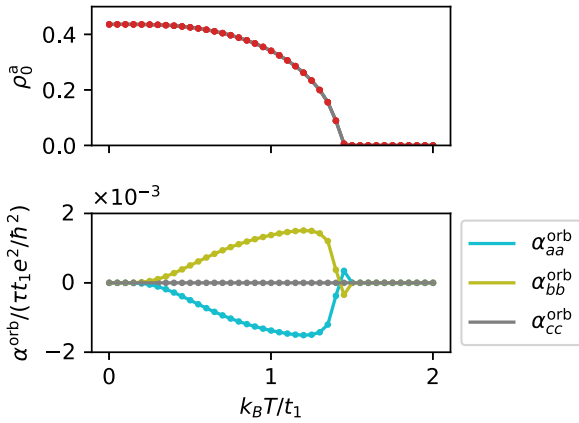

FIG. 5. Evolution of the magnetoelectric response through a phase transition with $g = 1.5t_1$ and $\rho = 0.5$. (Top panel) Order parameter ($\rho^{\mathrm{a}}_{\mathbf{Q}_0}$) as a function of temperature. (Bottom panel) Components of the OEE response tensor α^{orb} as a function of temperature. Components that are not shown are identically zero.

As seen in the lower panel of Fig. 5, the calculated α^{orb} is indeed of this form. The nonmonotonicity of α^{orb} is understood via the MF band structure, shown in Fig. 6. The top panel shows the high-temperature band structure; specifically, $k_{\mathrm{B}}T = 2.00\,t_1$. Although the system is in a metallic phase with many states within $k_{\mathrm{B}}T$ (gray shading) from the chemical potential μ (dashed line), in the high-symmetry phase, $\mathbf{m}_{\mathbf{k}n} = 0$ identically, so $\alpha^{\mathrm{orb}} = 0$. The middle panel shows the band structure at an intermediate temperature $k_{\mathrm{B}}T = 1.20\,t_1$ (near the peak in the α^{orb}); this is below the transition temperature, where the Phase-I charge order breaks inversion symmetry (along with the nonsymmorphic symmetries) and splits the bands throughout the Brillouin zone. The reduced symmetry of this phase allows gyrotropic response, so $\alpha^{\mathrm{orb}} \neq 0$. As the temperature is further lowered, the size of the band splitting increases and a full gap develops, with μ within this gap as expected at half filling (lower panel of Fig. 5). Hence, it is clear that in the low-temperature limit, as the sum in Eq. (6) approaches a Fermi-surface integral, α^{orb} should again vanish.

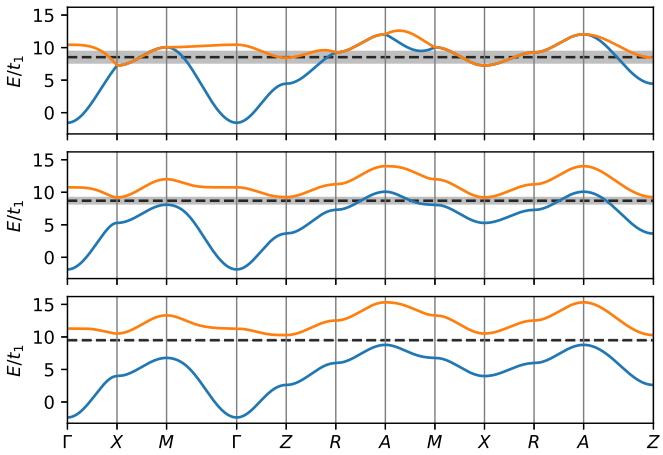

FIG. 6. Mean-field band structure at half filling (with parameters as specified in the main text) at three different temperatures: $k_{\mathrm{B}}T/t_1 = 2.00$ (top), 1.20 (middle), and 0.05 (bottom). The black dotted lines show the location of the chemical potential μ at each temperature, and the shaded areas centered at μ show the width $k_{\mathrm{B}}T$.

C. Role of line nodes

In this subsection, we inspect the contribution of the gapped-out line nodes to the magnetoelectric response tensor α^{orb} in Phase I. We find that these constitute the dominant sources of orbital magnetic moment $\mathbf{m}_{\mathbf{k}n}$ in the Brillouin zone and the dominant contribution to α^{orb}. First, we obtain analytical expressions for the orbital magnetic moment $\mathbf{m}_{\mathbf{k}n}$ in the vicinity of these nodes; then, we compare with data computed from the lattice model.

In Phase I, the charge order breaks the inversion symmetry Π (together with the nonsymmorphic symmetries); accordingly, in the MF Hamiltonian for Phase I, $d^3_{\mathbf{k}}$ is no longer constrained to be zero; hence the disappearance of the band touchings. Rather, $d^3_{\mathbf{k}}$ is set by the Phase-I order parameter $\rho^{\mathrm{a}}_{\mathbf{Q}_0}$. As a shorthand, define

$$\nu := \tilde{\rho}^{\mathrm{a}}_{\mathbf{Q}_0}, \tag{14}$$

where $\tilde{\rho}^{\mathrm{a}}_{\mathbf{Q}_0}$, defined in Appendix B, is proportional to the Phase-I order parameter $\rho^{\mathrm{a}}_{\mathbf{Q}_0}$.

In the high-symmetry phase, three independent line nodes exist in the first Brillouin zone (Fig. 2): (i) the X-R segment, (ii) the X-M segment, and (iii) the R-A segment—all other line nodes are related by the symmetry of Phase I. We expand about these (now-gapped) line nodes, denoting small deviations in momentum by $\tilde{\mathbf{k}}$. In the neighborhood of the (gapped) nodes, we have

(i) $k_a = \pi + \tilde{k}_a, \quad k_b = \tilde{k}_b, \quad -\pi < k_c \leqslant \pi$

$$d^0_{\mathbf{k}} = -2t_3 \cos(k_c) \tag{15a}$$
$$d^1_{\mathbf{k}} = 2(t_1 + (t_{2A} + t_{2B})\cos(k_c))\tilde{k}_a \tag{15b}$$
$$d^2_{\mathbf{k}} = 2(t_{2A} - t_{2B})\sin(k_c)\tilde{k}_b \tag{15c}$$
$$d^3_{\mathbf{k}} = \nu \tag{15d}$$

(ii) $-\pi < k_a < \pi, \quad k_b = \pi + \tilde{k}_b, \quad k_c = \tilde{k}_c$

$$d^0_{\mathbf{k}} = -2t_3 + 2t_1'(1 - \cos(k_a)) \tag{16a}$$
$$d^1_{\mathbf{k}} = 2(t_1 + t_{2A} + t_{2B})\cos\left(\frac{k_a}{2}\right)\tilde{k}_b \tag{16b}$$
$$d^2_{\mathbf{k}} = 4(t_{2A} - t_{2B})\sin\left(\frac{k_a}{2}\right)\tilde{k}_c \tag{16c}$$
$$d^3_{\mathbf{k}} = \nu \tag{16d}$$

(iii) $-\pi < k_a < \pi, \quad k_b = \pi + \tilde{k}_b, \quad k_c = \pi + \tilde{k}_c$

$$d^0_{\mathbf{k}} = 2t_3 + 2t_1'(1 - \cos(k_a)) \tag{17a}$$
$$d^1_{\mathbf{k}} = 2(t_1 - t_{2A} - t_{2B})\cos\left(\frac{k_a}{2}\right)\tilde{k}_b \tag{17b}$$
$$d^2_{\mathbf{k}} = -4(t_{2A} - t_{2B})\sin\left(\frac{k_a}{2}\right)\tilde{k}_c \tag{17c}$$
$$d^3_{\mathbf{k}} = \nu. \tag{17d}$$

For a two-band model with Bloch Hamiltonian $H_{\mathbf{k}} = d^0_{\mathbf{k}}\tau^0 + \vec{d}_{\mathbf{k}} \cdot \vec{\tau}$, $\mathbf{m}_{\mathbf{k}n}$ is the same for both bands and can be

written in the closed form [34,36]

$$m_{\mathbf{k}n,\kappa} = -\frac{e}{2\hbar}\sum_{\lambda\zeta}\varepsilon_{\kappa\lambda\zeta}\frac{\vec{d}_{\mathbf{k}}}{|\vec{d}_{\mathbf{k}}|^2}\cdot\left(\frac{\partial\vec{d}_{\mathbf{k}}}{\partial k_\lambda}\times\frac{\partial\vec{d}_{\mathbf{k}}}{\partial k_\zeta}\right), \tag{18}$$

where κ, λ, and ζ are Cartesian indices. In the neighborhood of a (gapped) line node in the $\hat{\mathbf{a}}$ direction, the Hamiltonian can generically be expressed as

$$d^0_{\mathbf{k}} = f(k_a), \quad \vec{d}_{\mathbf{k}} = (g_1(k_a)\tilde{k}_b,\ g_2(k_a)\tilde{k}_c,\ h(k_a)), \tag{19}$$

where f, g_1, g_2, and h are functions of k_a, and, hence, the components of $\mathbf{m}_{\mathbf{k}n}$ are given by

$$m_{\mathbf{k}n,a} = \frac{e}{2\hbar}\frac{1}{|\vec{d}_{\mathbf{k}}|^2}g_1g_2h \tag{20a}$$

$$m_{\mathbf{k}n,b} = \frac{e}{2\hbar}\frac{\tilde{k}_b}{|\vec{d}_{\mathbf{k}}|^2}g_2(g_1h' - g_1'h) \tag{20b}$$

$$m_{\mathbf{k}n,c} = \frac{e}{2\hbar}\frac{\tilde{k}_c}{|\vec{d}_{\mathbf{k}}|^2}g_1(g_2h' - g_2'h), \tag{20c}$$

where primes denote differentiation of the single-variable functions. To describe a line node in another direction, the indices in Eqs. (19) and (20) must be changed appropriately. We see that the longitudinal component $m_{\mathbf{k}n,a}$ is greatest at the (gapped) node itself (i.e., at $\tilde{k}_b = \tilde{k}_c = 0$, where $|\vec{d}_{\mathbf{k}}|^2$ is minimized), whereas the transverse components $m_{\mathbf{k}n,b}$ and $m_{\mathbf{k}n,c}$ are sizable in the neighborhood of the (gapped) node but vanish at the (gapped) node itself.

Figure 7 shows the orbital magnetic moment $m_{\mathbf{k}n,\kappa}$ as well as the product $-m_{\mathbf{k}n,\kappa}v_{\mathbf{k}n,\kappa}$ for bands $n \in \{1,2\}$ and components $\kappa \in \{a,b\}$ calculated from the lattice model—these are directly relevant to the nonvanishing components of α^{orb}. The parameters used are the same as for the middle panel of Fig. 6. As shown by Eq. (6), up to constant factors, the integrand for $\alpha^{\text{orb}}_{\kappa\kappa}$ is $-m_{\mathbf{k}n,\kappa}v_{\mathbf{k}n,\kappa}$ multiplied by $-df/d\xi|_{\xi=\varepsilon_{\mathbf{k}n}-\mu}$, a positive weighting factor concentrated within k_BT around the chemical potential μ. Hence, the equal-energy surfaces at $\varepsilon_{\mathbf{k}n} = \mu$ (solid black lines) and $\varepsilon_{\mathbf{k}n} = \mu \pm k_BT$ (dashed black lines) reveal the main contributions to the integral—generically, these are the (gapped) line nodes. In particular, at this temperature, for our choice of parameters, the largest contributions to α^{orb} are from the (gapped) line nodes at $k_c = \pm\pi$.

As outlined in Appendix D, the data of Fig. 7 reflects all the symmetries of the point group $\bar{4}2m$ of Phase I as well as time-reversal symmetry, which dictates $\mathbf{m}_{\mathbf{k}n} = -\mathbf{m}_{-\mathbf{k}n}$ and $\mathbf{v}_{\mathbf{k}n} = -\mathbf{v}_{-\mathbf{k}n}$. The large values of $\mathbf{m}_{\mathbf{k}n}$ are attributable to the presence of line nodes and are as expected from Eqs. 20: focusing on $m_{\mathbf{k}n,a}$, for the slices $k_c = \pm\pi/2$, we see the signature of line node (i) (transverse to $\hat{\mathbf{a}}$), for which $m_{\mathbf{k}n,a} \to 0$ in proximity to the node, and for the slices $k_c = 0$ and $k_c = \pm\pi$, we also recognize contributions from line nodes (ii) and (iii) (longitudinal to $\hat{\mathbf{a}}$), which are largest at the locus of the line nodes. The product $-m_{\mathbf{k}n,\kappa}v_{\mathbf{k}n,\kappa}$ still retains the general form of $m_{\mathbf{k}n,\kappa}$, though with a modified symmetry that allows a nonzero integral over the Fermi surface. The difference in the magnitude of the longitudinal contributions at $k_c = 0$ and $k_c = \pm\pi$ can be retraced to the different $g_1(k_a)$ for line nodes (ii) and (iii): while $g_1(k_a) = 2(t_1 + t_{2A} + t_{2B})\cos(k_a/2)$ for the former, $g_1(k_a) = 2(t_1 - t_{2A} - t_{2B})\cos(k_a/2)$ for the latter, and $|t_1 + t_{2A} + t_{2B}| > |t_1 - t_{2A} - t_{2B}|$ with our parameter values.

V. DISCUSSION AND CONCLUSION

It is sometimes overlooked that gyrotropy can arise without chiral or time-reversal symmetry breaking [23,43]. Since the point group $\bar{4}2m$ of the Phase-I order contains mirror symmetries (in our coordinates, one perpendicular to $\hat{\mathbf{x}}$ and another perpendicular to $\hat{\mathbf{y}}$), the ground state of this broken-symmetry phase is an example of a nonchiral gyrotropic structure. This is unlike many of the examples of the OEE studied so far [33,36], such as trigonal selenium and tellurium [20,35]. Furthermore, it constitutes a concrete example of longitudinal magnetization induced by a current in a mirror-symmetric structure, which had been implied to be disallowed by symmetry [33]. While longitudinal magnetization is forbidden by mirrors perpendicular or parallel to the current, it is not forbidden by mirrors at 45° angles from the current, such as those in Phase I.

Similarly to a previously studied model [36], a picture of current flowing through solenoidal paths in the crystal provides a qualitative understanding of the OEE in Phase I. Furthermore, this picture makes physically clearer why the OEE response vanishes (i) when $t_{2A} = t_{2B}$—hence giving an intuitive explanation for the necessity of assuming $t_{2A} \neq t_{2B}$ from the start—and (ii) in the absence of charge order, that is, when the atoms are indistinguishable. We imagine a current $\mathbf{j}$ driven in the $\hat{\mathbf{b}}$ direction: The simplest solenoidlike paths that result in net displacement purely in the $\hat{\mathbf{b}}$ direction are shown in Figs. 8 and 9.

(i) Each row of atoms, whether on sublattice A or B, is surrounded by a solenoid traced out of t_{2A} (green) hoppings and another traced out of t_{2B} (red) hoppings (Fig. 8). These two solenoids are of opposite helicities given the current $\mathbf{j}$, and if $t_{2A} = t_{2B}$, their induced magnetic fields cancel identically, precluding any current-induced magnetization whether in the symmetric phase or in a charge-ordered phase. Indeed, if $t_{2A} = t_{2B}$, there exist additional mirror planes (perpendicular to $\hat{\mathbf{a}}$ and to $\hat{\mathbf{b}}$) that interchange the two solenoids, but these mirrors are absent for $t_{2A} \neq t_{2B}$.

(ii) If $t_{2A} \neq t_{2B}$, let us presume without loss of generality that t_{2B} (in red) is dominant and ignore the t_{2A} solenoids. Figure 9 shows that, given the current $\mathbf{j}$, a solenoid whose central axis is a row of A sites is of helicity opposite to one whose central axis is a row of B sites. If the atoms on the two sublattices are indistinguishable, the magnetic fields induced by these two solenoids are equal and opposite and cancel when averaged over several lattice spacings. If the A and B atoms are distinguishable, however, the two sets of solenoids are distinct and can give rise to net magnetization. Indeed, the glide planes G_a and G_b (defined in Appendix C) of the symmetric phase interchange the dotted-line and solid-line solenoids; however, these glide planes are broken in Phase I.

It is surprising *a priori* that such a solenoid picture can exist in a nonchiral crystal (previous examples have focused on chiral structures and the helicity that naturally arises therefrom [20,33,36]); however, the two mirror symmetries of point group $\bar{4}2m$—one perpendicular to $\hat{\mathbf{x}}$ and the other

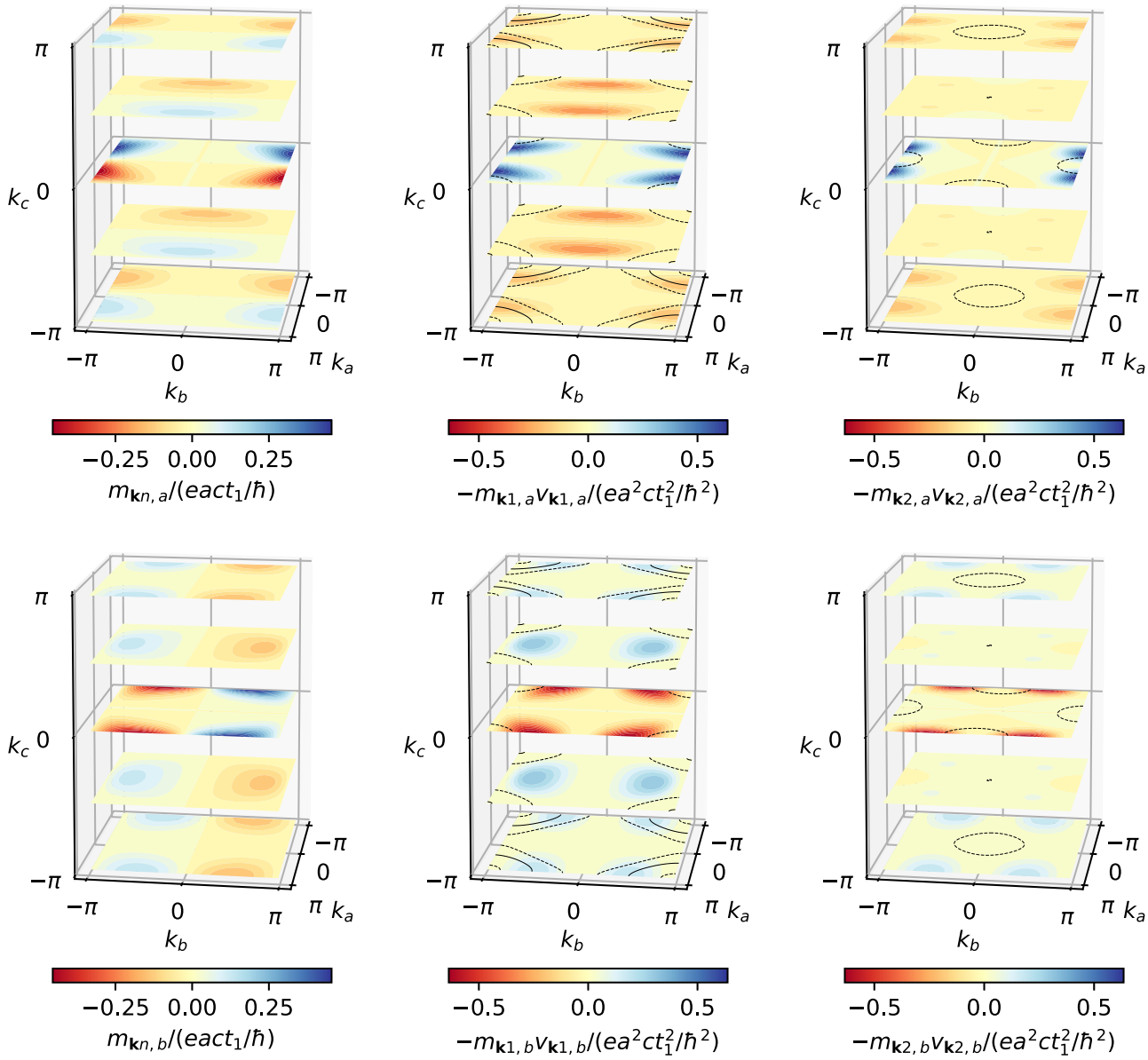

FIG. 7. Magnetic moment $m_{\mathbf{k}n,\kappa}$ and product $-m_{\mathbf{k}n,\kappa}v_{\mathbf{k}n,\kappa}$ for bands $n \in \{1, 2\}$ and components $\kappa \in \{a, b\}$ at $k_BT = 1.20\,t_1$. (Note that $\mathbf{m}_{\mathbf{k}n}$ is the same for both bands.) For clarity, the first Brillouin zone is not drawn to scale. The largest contributions to these two quantities are attributable to the line nodes depicted in Fig. 2. The solid lines in middle and right panels depict $\varepsilon_{\mathbf{k}n} = \mu$ surfaces. The dashed lines show $\varepsilon_{\mathbf{k}n} = \mu \pm k_BT$ surfaces, which delimit the region most heavily weighted in the integral of Eq. (13). The slices shown are $k_c = -\pi,\ -\pi/2,\ 0,\ \pi/2$, and π.

perpendicular to $\hat{\mathbf{y}}$—do not bring the solenoids into themselves, but rather exchange the $\hat{\mathbf{a}}$-axis solenoids with the $\hat{\mathbf{b}}$-axis solenoids. Hence, instead of forbidding a magnetoelectric response, the mirrors explain why the OEE coefficients along the $\hat{\mathbf{a}}$ and $\hat{\mathbf{b}}$ axes are opposite in sign, since the current is a polar vector and the magnetization is an axial vector.

In summary, we have discussed a simple model of a crystal with lines nodes and shown how charge order can lead to a nonzero OEE. Such an OEE could be probed by nuclear magnetic resonance experiments. We have also discussed how the magnetoelectric response has a large contribution arising from the vicinity of line nodes. Our work suggests that line node semimetals which are weakly gapped by charge order might be a promising place to search for large OEE.

Note added. Recently, we came across a theory preprint [52] which discusses the OEE induced by quadrupolar symmetry breaking in certain diamond lattice materials. While some of the ideas in that preprint overlap with our work, many of the details we consider (lattice structure, type of ordering, and line-node analysis) are significantly different.

ACKNOWLEDGMENTS

We thank D. A. Pesin for fruitful discussions. This research was funded by the Natural Sciences and Engineering Research Council of Canada and the Canadian Institute for Advanced Research. G.M. is supported by the *Fonds de recherche du Québec - Nature et technologies*. This research was enabled

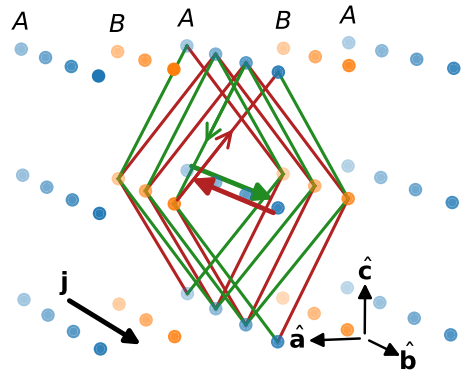

FIG. 8. For a current **j** oriented in the $\hat{\mathbf{b}}$ direction, solenoidlike paths due to the t_{2A} hoppings (green) and the t_{2B} hoppings (red) have opposite helicity. If $t_{2A} = t_{2B}$, the magnetizations from the two solenoids cancel. Crystal is not drawn to scale.

in part by support provided by Compute Ontario, Westgrid and Compute Canada. Computations were performed on the Niagara supercomputer at the SciNet HPC Consortium. SciNet is funded by the Canada Foundation for Innovation, the Government of Ontario, Ontario Research Fund - Research Excellence, and the University of Toronto.

APPENDIX A: CLASSICAL PHASE DIAGRAM

The charge ordered states favored by the interaction of Eq. (10) were identified by determining the energy of CDW modes in a classical picture of electrostatic charges by Fourier transforming and minimizing the repulsive interaction in momentum space. In Fig. 10, we show using which state has the lowest energy (according to V) as a function of the (relative) sizes of the repulsion strengths V_1, V_1', V_2, and V_3; the white star shows the relative parameter values used in the MF calculation. The ansatz for the mean-field theory described in the main text was chosen to potentially allow all the ground states that occur in this simplified model.

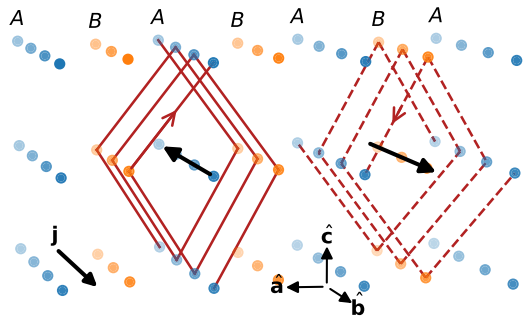

FIG. 9. For a current **j** oriented in the $\hat{\mathbf{b}}$ direction, solenoidlike paths with their axis along A atoms (solid lines) have opposite helicity to those with their axis along B atoms (dashed lines). If the atoms are indistinguishable, the magnetizations from the two solenoids cancel on average. Crystal is not drawn to scale.

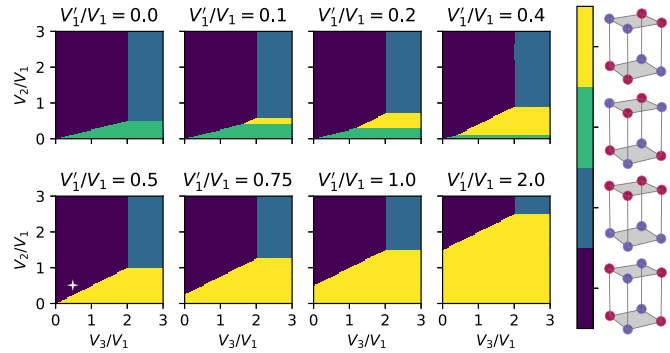

FIG. 10. Phase diagram showing the lowest-energy charge ordered states resulting from a model of electrostatic charges subject to the interaction of Eq. (10); the colors correspond to the indicated charge ordering patterns. The white star shows the relative parameter values used in the MF calculation.

APPENDIX B: DETAILS OF THE MEAN-FIELD CALCULATION

Here, we provide additional information regarding the self-consistent MF calculation of the CDW order. The electronic interaction of Eq. (10) was decomposed in the density channel, giving rise to the following MF interaction term:

$$V_{\mathrm{MF}} = \frac{1}{2} \sum_{(i,\alpha)\neq(j,\beta)} V_{ij}^{\alpha\beta} \left(\rho_i^{\alpha} n_j^{\beta} + n_i^{\alpha} \rho_j^{\beta} \right) \tag{B1a}$$

$$= N \sum_{\mathbf{q}}^{\mathrm{BZ}} \sum_{\alpha\beta} V_{\mathbf{q}}^{\alpha\beta} \rho_{\mathbf{q}}^{\alpha *} n_{\mathbf{q}}^{\beta}. \tag{B1b}$$

Here, N is the number of unit cells in the crystal, $\rho_{\mathbf{q}}^{\alpha} = N^{-1} \sum_i \mathrm{e}^{-i\mathbf{q}\cdot\mathbf{R}_i} \rho_i^{\alpha}$ (and likewise for $n_{\mathbf{q}}^{\alpha}$), and $V_{\mathbf{q}}^{\alpha\beta}$ is the Fourier transform of $V_{ij}^{\alpha\beta}$, which is invariant under simultaneous translation of i and j.

Choosing a closed set of commensurate wave vectors $\{\mathbf{Q}\}$ defines a *reduced Brillouin zone* (RBZ), which is mapped to the full Brillouin zone under addition of the wave vectors $\mathbf{Q}$. This property allows us to rewrite the integral of reciprocal-space-periodic functions as

$$\sum_{\mathbf{k}}^{\mathrm{BZ}} f(\mathbf{k}) = \sum_{\mathbf{Q}} \sum_{\mathbf{k}}^{\mathrm{RBZ}} f(\mathbf{k}+\mathbf{Q}), \tag{B2}$$

where the domain of the momentum sums is indicated above the summation symbol. Hence, we diagonalized the Hamiltonian $H_{\mathrm{MF}} = K + V_{\mathrm{MF}}$ in the RBZ by writing it in the form

$$K = \sum_{\mathbf{k}}^{\mathrm{RBZ}} \sum_{\alpha\beta} \sum_{\mathbf{Q}} c_{\mathbf{k}+\mathbf{Q}}^{\alpha\,\dagger} h_{\mathbf{k}+\mathbf{Q}}^{\alpha\beta} c_{\mathbf{k}+\mathbf{Q}}^{\beta} \tag{B3}$$

$$V_{\mathrm{MF}} = \sum_{\mathbf{k}}^{\mathrm{RBZ}} \sum_{\alpha} \sum_{\mathbf{Q}\mathbf{Q}'} c_{\mathbf{k}+\mathbf{Q}}^{\alpha\,\dagger} \tilde{\rho}_{\mathbf{Q}-\mathbf{Q}'}^{\alpha} c_{\mathbf{k}+\mathbf{Q}'}^{\alpha}, \tag{B4}$$

where $\tilde{\rho}_{\mathbf{Q}}^{\alpha} = \sum_{\beta} V_{\mathbf{Q}}^{\alpha\beta} \rho_{\mathbf{Q}}^{\beta}$ and $h_{\mathbf{k}}^{\alpha\beta}$ is the Bloch Hamiltonian, in our case given in Eq. (8) as $h_{\mathbf{k}} = d_{\mathbf{k}}^0 + \vec{d}_{\mathbf{k}} \cdot \vec{\tau}$. Starting from a series of randomized values for the MFs $\rho_{\mathbf{Q}}^{\alpha}$, we iterated until the computed expectation values agree with the input MFs to

within 10^{-6}. We compared the Helmholtz free energy F of the different ground states thusly obtained and selected the one with minimal F at every point in parameter space.

APPENDIX C: NONSYMMORPHIC SYMMETRIES AND PROTECTION OF THE GAPLESS LINES IN THE HIGH-SYMMETRY PHASE

In this Appendix, we show how the nonsymmorphic symmetries present in the space group $P4/nbm$ (that of the bare crystal in the absence of charge order) constrain the location of gapless lines via a Kramers-like degeneracy of the spinless fermions [53,54]. Three independent nonsymmorphic symmetries are present in the group. In Seitz notation and with respect to an origin at an inversion center, they are

$$G_a = \left\{ m_a \middle| \frac{\mathbf{b}}{2} \right\}, \tag{C1a}$$

$$G_b = \left\{ m_b \middle| \frac{\mathbf{a}}{2} \right\}, \tag{C1b}$$

$$G_c = \left\{ m_c \middle| \frac{\mathbf{a}+\mathbf{b}}{2} \right\}. \tag{C1c}$$

Each of these symmetries composed with time reversal gives rise to Kramers-like degeneracies along certain high-symmetry lines in momentum space. In order to obtain a Kramers-like degeneracy at momentum $\mathbf{k}$ due to an antiunitary operator $\tilde{\Theta}$, two conditions must be fulfilled: (i) $\tilde{\Theta}$ must map $\mathbf{k}$ to itself up to a reciprocal lattice vector, and (ii) for any $|\psi\rangle$ within the fixed-$\mathbf{k}$ subspace, we must have $\tilde{\Theta}^2 |\psi\rangle = -|\psi\rangle$ (that is, $\tilde{\Theta}$ must "square to -1").

For instance, under the action of $\tilde{\Theta} = \Theta G_a$,

$$\Theta G_a |k_a, k_b, k_c, \alpha\rangle = \begin{cases} |k_a, -k_b, -k_c, B\rangle^* & \alpha = A \\ \mathrm{e}^{-\mathrm{i}\mathbf{k}\cdot\mathbf{b}} |k_a, -k_b, -k_c, A\rangle^* & \alpha = B, \end{cases} \tag{C2}$$

while under the action of $\tilde{\Theta}^2 = (\Theta G_a)^2$,

$$(\Theta G_a)^2 |\mathbf{k}, \alpha\rangle = \mathrm{e}^{-\mathrm{i}k_b} |\mathbf{k}, \alpha\rangle \quad \forall\alpha, \tag{C3}$$

where $\mathbf{k} = k_a\hat{\mathbf{a}} + k_b\hat{\mathbf{b}} + k_c\hat{\mathbf{c}}$ and $|\mathbf{k}, \alpha\rangle = N^{-1/2} \sum_i \mathrm{e}^{-\mathrm{i}\mathbf{k}\cdot\mathbf{r}_i^\alpha} |i, \alpha\rangle$. It is then easy to see that the set of points at which conditions (i) and (ii) are fulfilled is

$$\{\mathbf{k} \in 1^{\mathrm{st}}\ \mathrm{BZ} \mid k_b = \pi \text{ and } k_c \in \{0, \pi\}\}. \tag{C4a}$$

Similarly, taking $\tilde{\Theta} = \Theta G_b$ and $\tilde{\Theta} = \Theta G_c$, respectively, gives Kramers-like degeneracies at momenta in the sets

$$\{\mathbf{k} \in 1^{\mathrm{st}}\ \mathrm{BZ} \mid k_b \in \{0, \pi\} \text{ and } k_c = \pi\} \tag{C4b}$$

and

$$\{\mathbf{k} \in 1^{\mathrm{st}}\ \mathrm{BZ} \mid (k_a, k_b) = (0, \pi) \text{ or } (k_a, k_b) = (\pi, 0)\}. \tag{C4c}$$

Hence, we have shown that the existence and location of the line nodes shown in Fig. 2 are determined by the nonsymmorphic symmetries of the space group combined with time reversal symmetry.

APPENDIX D: CRYSTAL CLASS $\bar{4}2m$

As stated in the main text, the (macroscopic) point group of Phase I is $\bar{4}2m$. With respect to the coordinates used above, the elements of the point group $\bar{4}2m$ are as follows.

(i) E, the identity;
(ii) $\bar{4}_c$ and $\bar{4}_c^{-1}$, a fourfold rotoinversion axis parallel to $\hat{\mathbf{c}}$ and its inverse, respectively;
(iii) $2_c = \bar{4}_c^2$, a twofold rotation axis parallel to $\hat{\mathbf{c}}$;
(iv) 2_a and 2_b, twofold rotation axes parallel to $\hat{\mathbf{a}}$ and $\hat{\mathbf{b}}$, respectively;
(v) m_{d_1} and m_{d_2}, mirror planes perpendicular to $(\hat{\mathbf{a}} + \hat{\mathbf{b}})/\sqrt{2}$ and $(\hat{\mathbf{a}} - \hat{\mathbf{b}})/\sqrt{2}$, respectively.

Under an (active) rigid-body transformation R, the axial rank-two tensor α transforms as [50]

$$\alpha_{\kappa\lambda} \to \alpha'_{\kappa\lambda} = \det(R) \sum_{\zeta\eta} R_{\kappa\zeta} R_{\lambda\eta} \alpha_{\zeta\eta}, \tag{D1}$$

where $\det(R) = 1$ for a transformation that preserves the parity of the axes and $\det(R) = -1$ for one that changes it. If $R \in \bar{4}2m$ [that is, R is a (macroscopic) symmetry of the crystal], then the response tensor must obey $\alpha = \alpha'$; this restricts the possible entries of the response tensor and, for $\bar{4}2m$, leads to the form shown in Eq. 13.

The point-group symmetry also constrains the form of the polar vector $\mathbf{v}_{\mathbf{k}n}$ and of the axial vector $\mathbf{m}_{\mathbf{k}n}$. For any transformation R in the point group,

$$\mathbf{v}_n(\mathbf{k}) = R\,\mathbf{v}_n(R^{-1}\mathbf{k}) \tag{D2a}$$

$$\mathbf{m}_n(\mathbf{k}) = \det(R) R\,\mathbf{m}_n(R^{-1}\mathbf{k}), \tag{D2b}$$

where we have used functional notation for the crystal momenta in order to avoid excessive indexing.

For example, if $R = \bar{4}_c$, then

$$\bar{4}_c\mathbf{k} = \begin{pmatrix} k_b \\ -k_a \\ -k_c \end{pmatrix}, \tag{D3}$$

and so

$$\begin{pmatrix} v_{n,a}(\mathbf{k}) \\ v_{n,b}(\mathbf{k}) \\ v_{n,c}(\mathbf{k}) \end{pmatrix} = \begin{pmatrix} +v_{n,b}(\bar{4}_c^{-1}\mathbf{k}) \\ -v_{n,a}(\bar{4}_c^{-1}\mathbf{k}) \\ -v_{n,c}(\bar{4}_c^{-1}\mathbf{k}) \end{pmatrix} \tag{D4a}$$

$$\begin{pmatrix} m_{n,a}(\mathbf{k}) \\ m_{n,b}(\mathbf{k}) \\ m_{n,c}(\mathbf{k}) \end{pmatrix} = \begin{pmatrix} -m_{n,b}(\bar{4}_c^{-1}\mathbf{k}) \\ +m_{n,a}(\bar{4}_c^{-1}\mathbf{k}) \\ +m_{n,c}(\bar{4}_c^{-1}\mathbf{k}) \end{pmatrix}. \tag{D4b}$$

This and other constraints are consistent with the data of Fig. 7, as is clear by inspection.

[1] N. A. Spaldin and M. Fiebig, The renaissance of magnetoelectric multiferroics, Science **309**, 391 (2005).
[2] W. Eerenstein, N. D. Mathur, and J. F. Scott, Multiferroic and magnetoelectric materials, Nature (London) **442**, 759 (2006).
[3] R. Ramesh and N. A. Spaldin, Multiferroics: Progress and prospects in thin films, Nat. Mater. **6**, 21 (2007).
[4] S.-W. Cheong and M. Mostovoy, Multiferroics: A magnetic twist for ferroelectricity, Nat. Mater. **6**, 13 (2007).

[5] N. A. Spaldin, S.-W. Cheong, and R. Ramesh, Multiferroics: Past, present, and future, Phys. Today **63**(10), 38 (2010).

[6] G. Lawes and G. Srinivasan, Introduction to magnetoelectric coupling and multiferroic films, J. Phys. D **44**, 243001 (2011).

[7] L. E. Fuentes-Cobas, J. A. Matutes-Aquino, M. E. Botello-Zubiate, A. González-Vázquez, M. E. Fuentes-Montero, and D. Chateigner, Advance in magnetoelectric materials and their application, in *Handbook of Magnetic Materials*, edited by K. H. J. Buschow, Vol. 24 (Elsevier, New York, 2015), Chap. 3, pp. 237–322.

[8] Z. Chu, M. PourhosseiniAsl, and S. Dong, Review of multi-layered magnetoelectric composite materials and devices applications, J. Phys. D **51**, 243001 (2018).

[9] M. Z. Hasan and C. L. Kane, Colloquium: Topological insulators, Rev. Mod. Phys. **82**, 3045 (2010).

[10] X.-L. Qi and S.-C. Zhang, Topological insulators and superconductors, Rev. Mod. Phys. **83**, 1057 (2011).

[11] A. G. Grushin and F. de Juan, Finite-frequency magnetoelectric response of three-dimensional topological insulators, Phys. Rev. B **86**, 075126 (2012).

[12] D. A. Pesin and A. H. MacDonald, Topological Magnetoelectric Effect Decay, Phys. Rev. Lett. **111**, 016801 (2013).

[13] D. Schmeltzer and A. Saxena, Magnetoelectric effect induced by electron–electron interaction in three dimensional topological insulators, Phys. Lett. A **377**, 1631 (2013).

[14] A. G. Mal'Shukov, H. Skarsvåg, and A. Brataas, Nonlinear magneto-optical and magnetoelectric phenomena in topological insulator heterostructures, Phys. Rev. B **88**, 245122 (2013).

[15] D. Baasanjav, O. A. Tretiakov, and K. Nomura, Magnetoelectric effect in topological insulator films beyond the linear response regime, Phys. Rev. B **90**, 045149 (2014).

[16] T. Morimoto, A. Furusaki, and N. Nagaosa, Topological magnetoelectric effects in thin films of topological insulators, Phys. Rev. B **92**, 085113 (2015).

[17] D. Xiao, J. Jiang, J.-H. Shin, W. Wang, F. Wang, Y.-F. Zhao, C. Liu, W. Wu, M. H. W. Chan, N. Samarth, and C.-Z. Chang, Realization of the Axion Insulator State in Quantum Anomalous Hall Sandwich Heterostructures, Phys. Rev. Lett. **120**, 056801 (2018).

[18] Y. Tokura, K. Yasuda, and A. Tsukazaki, Magnetic topological insulators, Nat. Rev. Phys. **1**, 126 (2019).

[19] L. S. Levitov, Yu. V. Nazarov, and G. M. Eliashberg, Magnetoelectric effects in conductors with mirror isomer symmetry, Zh. Eksp. Teor. Fiz. **88**, 229 (1985) [Sov. Phys. JETP **61**, 133 (1985)].

[20] C. Şahin, J. Rou, J. Ma, and D. A. Pesin, Pancharatnam-Berry phase and kinetic magnetoelectric effect in trigonal tellurium, Phys. Rev. B **97**, 205206 (2018).

[21] J. Sinova, S. O. Valenzuela, J. Wunderlich, C. H. Back, and T. Jungwirth, Spin Hall effects, Rev. Mod. Phys. **87**, 1213 (2015).

[22] A. Manchon, H. C. Koo, J. Nitta, S. M. Frolov, and R. A. Duine, New perspectives for Rashba spin–orbit coupling, Nat. Mater. **14**, 871 (2015).

[23] S. D. Ganichev, M. Trushin, and J. Schliemann, Spin polarization by current, in *Handbook of Spin Transport and Magnetism*, edited by Evgeny Y. Tsymbal and Igor Zutic, 2nd ed. (Chapman and Hall/CRC, Boca Raton, 2016), pp. 504–513.

[24] Y. K. Kato, R. C. Myers, A. C. Gossard, and D. D. Awschalom, Current-Induced Spin Polarization in Strained Semiconductors, Phys. Rev. Lett. **93**, 176601 (2004).

[25] A. Y. Silov, P. A. Blajnov, J. H. Wolter, R. Hey, K. H. Ploog, and N. S. Averkiev, Current-induced spin polarization at a single heterojunction, Appl. Phys. Lett. **85**, 5929 (2004).

[26] Y. K. Kato, R. C. Myers, A. C. Gossard, and D. D. Awschalom, Electrical initialization and manipulation of electron spins in an L-shaped strained *n*-InGaAs channel, Appl. Phys. Lett. **87**, 022503 (2005).

[27] V. Sih, R. C. Myers, Y. K. Kato, W. H. Lau, A. C. Gossard, and D. D. Awschalom, Spatial imaging of the spin Hall effect and current-induced polarization in two-dimensional electron gases, Nat. Phys. **1**, 31 (2005).

[28] N. P. Stern, S. Ghosh, G. Xiang, M. Zhu, N. Samarth, and D. D. Awschalom, Current-Induced Polarization and the Spin Hall Effect at Room Temperature, Phys. Rev. Lett. **97**, 126603 (2006).

[29] C. L. Yang, H. T. He, L. Ding, L. J. Cui, Y. P. Zeng, J. N. Wang, and W. K. Ge, Spectral Dependence of Spin Photocurrent and Current-Induced Spin Polarization in an InGaAs/InAlAs Two-Dimensional Electron Gas, Phys. Rev. Lett. **96**, 186605 (2006).

[30] H. J. Zhang, S. Yamamoto, Y. Fukaya, M. Maekawa, H. Li, A. Kawasuso, T. Seki, E. Saitoh, and K. Takanashi, Current-induced spin polarization on metal surfaces probed by spin-polarized positron beam, Sci. Rep. **4**, 4844 (2014).

[31] V. A. Shalygin, A. N. Sofronov, L. E. Vorob'ev, and I. I. Farbshtein, Current-induced spin polarization of holes in tellurium, Phys. Solid State **54**, 2362 (2012).

[32] T. Furukawa, Y. Shimokawa, K. Kobayashi, and T. Itou, Observation of current-induced bulk magnetization in elemental tellurium, Nat. Commun. **8**, 954 (2017).

[33] T. Yoda, T. Yokoyama, and S. Murakami, Current-induced orbital and spin magnetizations in crystals with helical structure, Sci. Rep. **5**, 12024 (2015).

[34] S. Zhong, J. E. Moore, and I. Souza, Gyrotropic Magnetic Effect and the Magnetic Moment on the Fermi Surface, Phys. Rev. Lett. **116**, 077201 (2016).

[35] J. Rou, C. Şahin, J. Ma, and D. A. Pesin, Kinetic orbital moments and nonlocal transport in disordered metals with nontrivial band geometry, Phys. Rev. B **96**, 035120 (2017).

[36] T. Yoda, T. Yokoyama, and S. Murakami, Orbital Edelstein effect as a condensed-matter analog of solenoids, Nano Lett. **18**, 916 (2018).

[37] S. S. Tsirkin, P. A. Puente, and I. Souza, Gyrotropic effects in trigonal tellurium studied from first principles, Phys. Rev. B **97**, 035158 (2018).

[38] F. Flicker, F. de Juan, B. Bradlyn, T. Morimoto, M. G. Vergniory, and A. G. Grushin, Chiral optical response of multifold fermions, Phys. Rev. B **98**, 155145 (2018).

[39] C. Niu, J.-P. Hanke, P. M. Buhl, H. Zhang, L. Plucinski, D. Wortmann, S. Blügel, G. Bihlmayer, and Y. Mokrousov, Mixed topological semimetals driven by orbital complexity in two-dimensional ferromagnets, Nat. Commun. **10**, 3179 (2019).

[40] L.-K. Shi and J. C. W. Song, Symmetry, spin-texture, and tunable quantum geometry in a WTe_2 monolayer, Phys. Rev. B **99**, 035403 (2019).

[41] A. Silva, J. Henke, and J. van Wezel, Elemental chalcogens as a minimal model for combined charge and orbital order, Phys. Rev. B **97**, 045151 (2018).

[42] M. Gradhand and J. van Wezel, Optical gyrotropy and the nonlocal Hall effect in chiral charge-ordered $TiSe_2$, Phys. Rev. B **92**, 041111 (2015).

[43] J. Orenstein and J. E. Moore, Berry phase mechanism for optical gyrotropy in stripe-ordered cuprates, Phys. Rev. B **87**, 165110 (2013).

[44] R. Resta, Electrical polarization and orbital magnetization: The modern theories, J. Phys.: Condens. Matter **22**, 123201 (2010).

[45] T. Thonhauser, Theory of orbital magnetization in solids, Int. J. Mod. Phys. B **25**, 1429 (2011).

[46] D. Vanderbilt, *Berry Phases in Electronic Structure Theory: Electric Polarization, Orbital Magnetization and Topological Insulators* (Cambridge University Press, Cambridge, 2018).

[47] R. Resta, Electrical polarization and orbital magnetization: The position operator tamed, edited by W. Andreoni and S. Yip, in *Handbook of Materials Modeling: Methods: Theory and Modeling* (Springer International Publishing, Cham, 2018), pp. 1–31.

[48] D. Xiao, M.-C. Chang, and Q. Niu, Berry phase effects on electronic properties, Rev. Mod. Phys. **82**, 1959 (2010).

[49] N. W. Ashcroft and N. D. Mermin, *Solid State Physics* (Holt, Rinehart and Winston, New York, 1976).

[50] J. F. Nye, *Physical Properties of Crystals: Their Representation by Tensors and Matrices* (Oxford University Press, New York, 1985).

[51] L. D. Landau and E. M. Lifshitz, *Electrodynamics of Continuous Media*, Course of Theoretical Physics, Vol. 8 (Pergamon Press, New York, 1960).

[52] T. Ishitobi and K. Hattori, Magnetoelectric Effects and Charge-Imbalanced Solenoids: Antiferro Quadrupole Orders in a Diamond Structure, J. Phys. Soc. Jpn. **88**, 063708 (2019).

[53] S. M. Young and C. L. Kane, Dirac Semimetals in two Dimensions, Phys. Rev. Lett. **115**, 126803 (2015).

[54] W. Choi, T. Mizoguchi, and Y. B. Kim, Symmetry-protected topological magnons in three dimensional Kitaev materials, arXiv:1903.02559.